

RESEARCH LETTER

10.1002/2014GL059284

Key Points:

- Applied high-fidelity LES to model oil dilution in ocean mixed layer
- Reproduced various observed oil dilution patterns, from fingered to diffused
- Introduced a nondimensional parameter to characterize modes of oil dilution

Supporting Information:

- Text S1 and Figures S1–S4

Correspondence to:

C. Meneveau,
meneveau@jhu.edu

Citation:

Yang, D., M. Chamecki, and C. Meneveau (2014), Inhibition of oil plume dilution in Langmuir ocean circulation, *Geophys. Res. Lett.*, *41*, 1632–1638, doi:10.1002/2014GL059284.

Received 14 JAN 2014

Accepted 8 FEB 2014

Accepted article online 14 FEB 2014

Published online 6 MAR 2014

Corrected 2 JUN 2014

This article was corrected on 2 JUN 2014. See the end of the full text for details.

Inhibition of oil plume dilution in Langmuir ocean circulation

Di Yang¹, Marcelo Chamecki², and Charles Meneveau¹¹Center for Environmental and Applied Fluid Mechanics, Johns Hopkins University, Baltimore, Maryland, USA,²Department of Meteorology, Pennsylvania State University, University Park, Pennsylvania, USA

Abstract Oil spills from deep-water blowouts rise through and interact with the ocean mixed layer and Langmuir turbulence, leading to considerable diversity of oil slick dilution patterns observed on the ocean surface. Certain conditions can drive oil droplet plumes to organize into distinct bands called windrows, inhibiting oil dilution. Observations of blurred or even diffused plumes are also common, but conditions under which these various dilution regimes emerge are not well understood. Here we use large eddy simulations to explain and quantify the dilution patterns and their dependence on relevant physical parameters. Two mechanisms, the downwelling and dilution due to Langmuir cells and the inhibition of dilution due to buoyancy of oil droplets, compete. This competition can be characterized by the ratio of Stokes drift to droplet rise velocity—the drift-to-buoyancy parameter, Db . We find that plume appearance and quantitative measures of relative dilution depend mainly on Db .

1. Introduction

The ocean mixed layer (OML) is governed by many physical processes, among which the Langmuir ocean circulation [Langmuir, 1938] plays a critical role in enhancing ocean mixing as well as organizing buoyant particles [Okubo, 1970; Leibovich, 1983; Moum and Smyth, 2001; Thorpe, 2004; Edson et al., 2007; Sullivan and McWilliams, 2010]. The combined effect of horizontal convergence and buoyancy forces causes oil droplets and bubbles to accumulate in fingers along the windrows on the ocean surface, as often observed in aerial photos (Figure 1a) [see e.g., Li, 2000; Rye, 2000; Thorpe, 2004; Leifer et al., 2012]. The oil dilution within such fingers is clearly inhibited. We remark that without the presence of Langmuir circulation, surface floaters are usually clustered into patches instead of fingers [Skylingstad and Denbo, 1995; Noh et al., 2006; Teixeira and Belcher, 2010].

Langmuir circulations and turbulence in the OML are both driven by the wind. Wind generates waves on the ocean surface, resulting in an averaged Stokes drift current $u_s(z \leq 0) = U_s \exp(2kz)$ along the wave propagation direction [Stokes, 1847], where U_s is its magnitude and k is the wavenumber, and z is depth. Meanwhile, the wind stress generates a vertical shear in the ocean mixed layer, for which the friction velocity is $u_* = \sqrt{\tau_s/\rho}$ where τ_s is the surface stress and ρ is the sea water density. The interaction between Stokes drift and wind-driven shear produces a vortex force that generates the Langmuir circulations [Craik and Leibovich, 1976]. These flow structures consist of slow, counter-rotating vortex pairs aligned with the mean wind direction, which induce horizontal convergence of surface fluids into the windrows as well as downwelling underneath the windrows [Langmuir, 1938; Leibovich, 1983; Thorpe, 2004]. The relative strength of Langmuir circulation and shear turbulence is measured by the turbulent Langmuir number $La_t = \sqrt{u_*}/U_s$ [McWilliams et al., 1997].

The fingered slick patterns seen in Figure 1a do not always occur [Rye, 2000; Leifer et al., 2012]. Instead, two additional types of oil slick patterns are also frequently observed, i.e., fingers with blurred gaps (Figure 1b) and diluted slicks (Figure 1c). The lack of physical understanding and quantitative description of such diverse patterns of oil slick dilution has prevented the development of parameterizations to include effects of Langmuir circulation in the oil spill prediction models [Simecek-Beatty and Lehr, 2000]. This in turn hampers accurate predictions of oil dilution in the OML, leading to inaccurate estimates of biodegradation of oil spills [Camilli et al., 2010; Hazen et al., 2010] and possibly compromising plans for remediation. Moreover, high-resolution remote sensing images provide valuable information on the surface oil slicks [Leifer et al., 2012; Garcia-Pineda et al., 2013], but better understanding of the dynamics causing different surface patterns is needed in order to improve the interpretation of remotely sensed surface imagery of oil slicks. To increase our understanding, in this study, we (i) identify the dominant physical processes that govern the

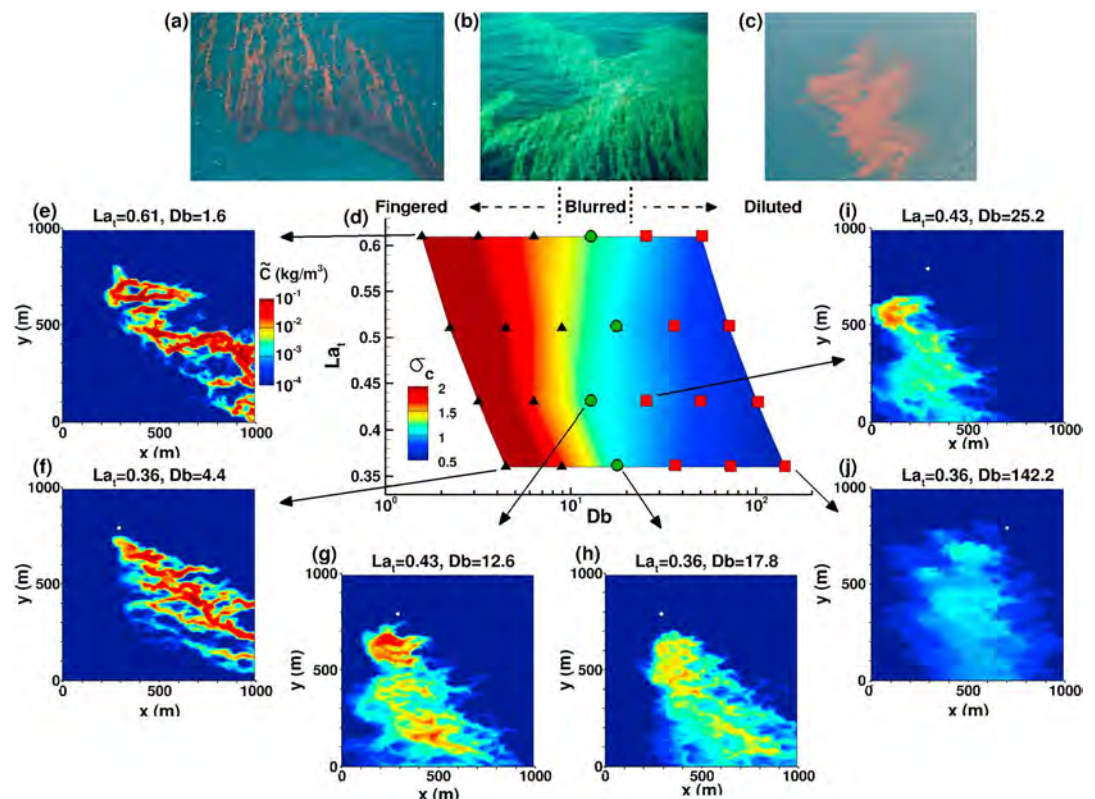


Figure 1. Dispersion regimes for surface oil slicks from underwater blowouts. (a–c) Field images of surface oil slicks. (d) Fingering level σ_c as a function of Db and La_t . (e–j) Contours of \tilde{C} on the surface obtained from the LES, where the white dot indicates the horizontal location of the underwater releasing source. In Figure 1d, the surface oil slicks from the 24 LES cases are categorized into three regimes: black triangle, fingered ($Db \lesssim 10$); green circle, blurred ($10 \lesssim Db \lesssim 25$); and reds square, diluted ($Db \gtrsim 25$). For Figure 1a, photo credited to U.S. Air Force photo/Tech. Sgt. Adrian Cadiz; for Figure 1b, photo credited to NOAA Hazardous Materials Response Division, now NOAA office of Response and Restoration; for Figure 1c, photo credited to National Wildlife Federation/NWF.org.

dilution of oil spills in Langmuir turbulence; (ii) formulate a new dimensionless parameter that indicates the transitions between different slick patterns, and (iii) quantify the oil dilution level as a function of the new parameter and La_t .

While Langmuir circulation inhibits dilution of surface floaters, it also increases vertical mixing of tracer particles [McWilliams and Sullivan, 2000]. Therefore, for the oil droplets to stay in the windrows, the hydrodynamic forces induced by downwelling need to be overcome by the buoyancy force acting on oil droplets. The problem can be addressed by comparing two velocity scales, the droplet rise velocity w_r , and the downwelling velocity associated with Langmuir circulation. The latter depends in complicated ways upon the Stokes drift velocity U_s , which drives the creation of Langmuir cells. Since in our study we will treat the Stokes drift velocity U_s as the relevant independent parameter we propose a new dimensionless quantity, the drift-to-buoyancy parameter,

$$Db = \frac{U_s}{w_r}, \quad (1)$$

to measure the relative strength of the downwelling velocity (dependent on U_s) bringing droplets into the OML, and the rise velocity keeping droplets on the surface. Db will be used to separate regimes in which Langmuir circulation enhances mixing from those in which it inhibits dilution by forming surface fingers of oil droplets along the windrows.

2. Large Eddy Simulation

We use large eddy simulation (LES) to model oil dispersion in the OML under varying conditions of wind shear, surface wave characteristics, and oil droplet sizes. LES is capable of producing high-fidelity

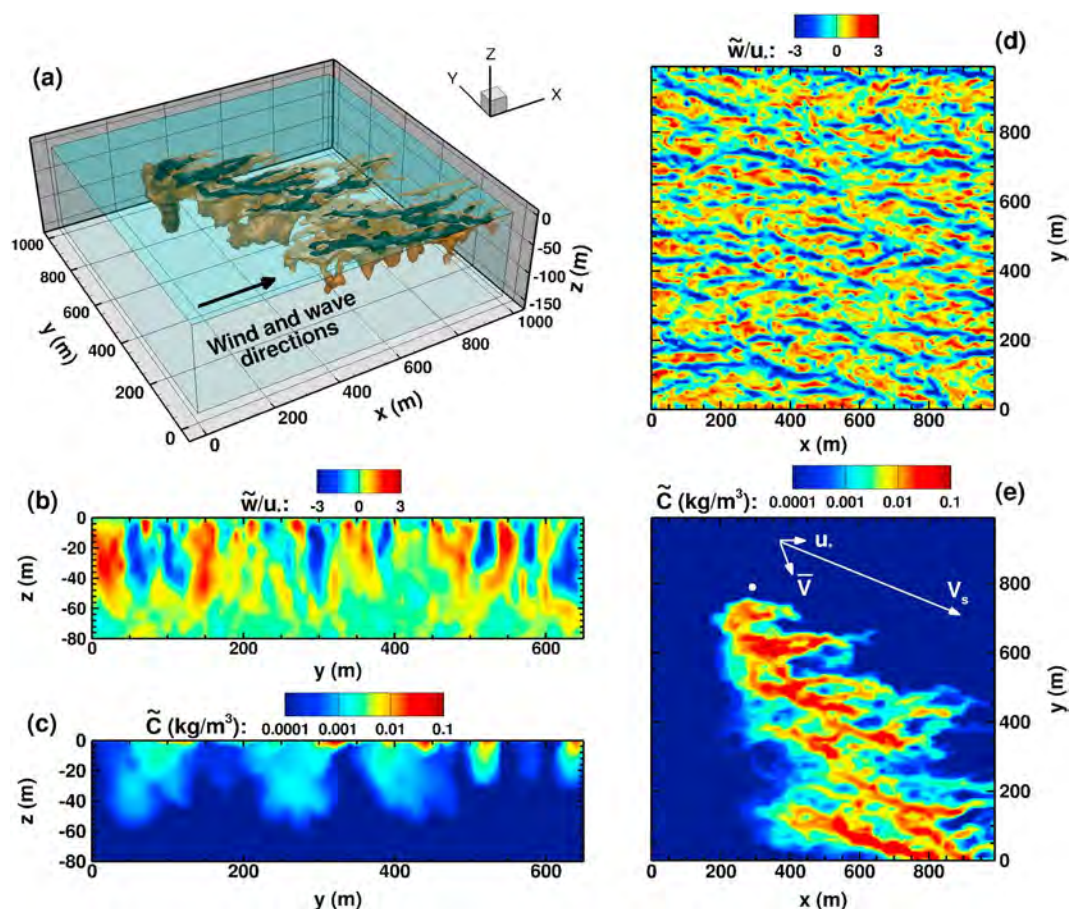


Figure 2. Overview of LES results modeling oil spill dispersion in the ocean mixed layer with the presence of Langmuir circulation. Case $(La_t, Db) = (0.43, 6.3)$ is shown. (a) Three-dimensional isosurfaces of $\tilde{C} = 0.008 \text{ kg/m}^3$ (brown) and 0.016 kg/m^3 (black). (b) Contours of \tilde{w} at $x = 500 \text{ m}$. (c) Contours of \tilde{C} at $x = 500 \text{ m}$. (d) Contours of \tilde{w} at $z = -10 \text{ m}$. (e) Contours of \tilde{C} at $z = 0 \text{ m}$. In Figure 2e, reference vectors for friction velocity u_* , mean surface flow velocity V_s , and mean depth-averaged (over OML) flow velocity \bar{V} are plotted.

representations of Langmuir circulations and large-to-moderate scale turbulent eddies [Skylingstad and Denbo, 1995; McWilliams et al., 1997]. Only the small eddies must be represented by a subgrid-scale model.

The LES model we use for the ocean mixed layer is based on the filtered Craik–Leibovich (CL) equations [Leibovich, 1980, 1983; Craik, 1985]. It accounts for the phase-averaged effects of surface gravity waves on the mean flow and turbulence by including a (uniform and constant) Stokes drift term. We note that there are several other physical mixing processes that may influence the oil dilution, e.g., breaking waves, submesoscale eddies and filaments, and precipitation [Edson et al., 2007]. In the present study we opt to omit these effects to aid in the interpretation of simulation results. In recent years, CL-based LES has been widely adopted as the prevailing numerical model for simulating Langmuir turbulence [e.g., Skylingstad and Denbo, 1995; McWilliams et al., 1997; McWilliams and Sullivan, 2000; Li et al., 2005; Noh et al., 2006; Harcourt and D’Asaro, 2008; Kukulka et al., 2009]. The concentration field of oil droplets is described by a Eulerian concentration field $C(x, y, z, t)$, with the oil droplet velocity being modeled by accounting for the additional contributions from the buoyancy and inertia of the droplets [Chamecki et al., 2008, 2009; Chamecki and Meneveau, 2011; Pan et al., 2013]. The buoyancy effect of both density fluctuations (represented by a potential temperature field) and oil droplet concentration is included into the momentum equation based on the Boussinesq approximation.

In the simulations (Figure 2) we consider a mean wind speed of $U_{10} = 10 \text{ m/s}$ at 10 m above the mean sea surface, corresponding to a friction velocity of approximately $u_* = 0.0125 \text{ m/s}$ in the ocean mixed layer. Under the forcing of a steady wind, the wind-generated waves can have various wavelengths and amplitudes depending on the fetch along which wind acts on the waves [Hasselmann et al., 1973]. Here we

consider four wave conditions with the corresponding turbulent Langmuir numbers $La_t = 0.61, 0.51, 0.43,$ and 0.36 . Smaller La_t corresponds to stronger wave forcing, so that stronger Langmuir turbulence and larger downwelling velocities are expected (Figure S1 in the supporting information).

We adopt $\rho = 1031.0 \text{ kg/m}^3$, the density of oil $\rho_d = 859.9 \text{ kg/m}^3$, and the viscosity of sea water $\mu_f = 1.08 \times 10^{-3} \text{ kg/(m s)}$. The oil is released from a localized source (at $z = -150 \text{ m}$) in the lower portion of the simulation domain below the thermocline with a releasing rate $Q_s = 1 \text{ kg/s}$. For each Langmuir turbulence condition, we consider six different oil droplet diameters, $d(n = 1 \sim 6) = 88.4 \times 2^{(n-1)/2} \mu\text{m}$. The corresponding rise velocity is given by Stokes' law, i.e., $w_r = (\rho_d - \rho)gd^2 / (18\mu_f)$. These droplet sizes cover a wide range the drift-to-buoyancy parameter Db , from 1.6 to 142.2 . Figure 1d illustrates the (Db, La_t) parameter space in which each LES case is denoted by a solid symbol. Several typical snapshots of the surface plume from the LES are shown as well. Even though a one-to-one comparison between simulations and observations in Figure 1 is not possible, LES clearly captures the transition from fingered plumes in which most of the surface oil is concentrated in narrow fingers to diluted plumes where no fingers are visible. More details about the LES model, the wave parameters, the droplet rise velocity, and the setup of the simulations are available in the supporting information.

3. Results and Discussion

As shown in Figure 2a, the oil droplets initially rise through a narrow and nearly vertical plume. After crossing the thermocline (about 80 m deep), the stirring effect by the Ekman spiral as well as the turbulent mixing in the OML cause the oil plume to twist and expand horizontally. When the plume reaches the surface layer where Langmuir circulations dominate, the oil droplets are quickly advected into the windrows, which are indicated by the narrow streamwise bands with strong negative vertical velocity (Figure 2d). After this, the horizontal shear and the downwelling flow associated with the counter-rotating Langmuir cells tend to tear off the oil droplets from the surface slicks and transport them back to deeper water. For the case $Db = 6.3$ illustrated in Figure 2, the buoyancy force on the oil droplets is able to overcome the downward force due to Langmuir turbulence, so that most of the oil droplets remain near the surface and concentrate in the windrows. The correlation between the resolved vertical velocity \tilde{w} and the resolved oil concentration \tilde{C} can be observed in Figures 2b–2e.

In the Northern Hemisphere and under ideal conditions, the theoretical solution of the Ekman spiral predicts surface transport 45° and a net transport 90° clockwise from the mean wind direction (i.e., along the $-y$ direction in the frame of our simulations) when averaged over the Ekman layer [Ekman, 1905]. When Stokes drift is included, the Ekman spiral is modified with enhanced downwind surface transport [McWilliams et al., 1997]. The overall surface oil plume pattern in Figure 2e reflects such mean transport effect. We remark that the theoretical solutions [Ekman, 1905; McWilliams et al., 1997] and the current LES of the Ekman transport correspond to a steady state response to the wind stress and the Coriolis effect. Under fully realistic field conditions, other effects such as the unsteadiness of the wind and buoyancy-driven convection further complicate the Ekman transport [Lenn and Chereskin, 2009]. These effects are beyond the scope of the current study.

The presence of Langmuir circulation can have important consequences for oil transport, because the downwind velocity in the windrows exceeds the average velocity on the surface [Thorpe, 2004]. If the buoyancy force is small (i.e., the cases with $Db \gtrsim 25$), the oil droplets are diluted over the ocean mixed layer and are transported more crosswind (e.g., Figure 1j). If the buoyancy force is large (i.e., the cases with $Db \lesssim 10$), the oil droplets can stay in the windrows. There, the dilution is significantly inhibited and the oil is transported more downwind (e.g., Figure 1f).

In order to describe quantitatively the level of fingering (or inhibition of dilution), we use the normalized root-mean-square (RMS) of the temporal fluctuation of surface oil concentration σ_c . First, the time-averaged oil concentration $\bar{C}(x, y, z)$ is calculated. The corresponding temporal fluctuation is thus given by $\tilde{C}'(x, y, z, t) = \tilde{C}(x, y, z, t) - \bar{C}(x, y, z)$. The locally normalized RMS of the temporal fluctuation is $\tilde{C}'_{\text{RMS}}(x, y, z) = \tilde{C}'_{\text{RMS}}(x, y, z) / \bar{C}(x, y, z)$ if $\bar{C} > 10^{-4} \text{ kg/m}^3$ and zero otherwise, where \tilde{C}'_{RMS} is the standard RMS of \tilde{C}' . Based on the above calculations, the fingering level parameter σ_c is defined as $\sigma_c = (N_{xy}^{(p)})^{-1} \sum_{i=1}^{N_x} \sum_{j=1}^{N_y} \tilde{C}'_{\text{RMS}}(x(i), y(j), z = 0)$, where N_x and N_y are, respectively, the total number of computational grid points in x and y directions, and $N_{xy}^{(p)}$ is the total number of surface grid points where

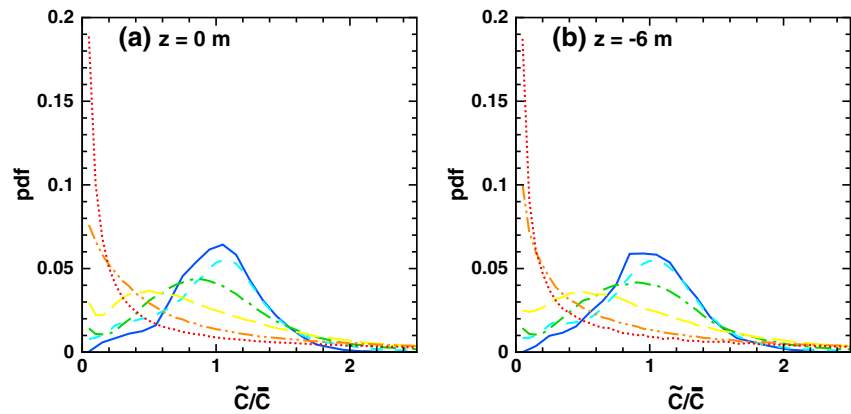


Figure 3. Probability density function of normalized surface oil concentration \tilde{C}/\bar{C} . (a) PDFs at $z = 0$ m and (b) PDFs at $z = -6$ m. The LES results for Langmuir turbulence of $La_t = 0.36$ are shown. Results for various droplet diameters are plotted: dotted lines, $Db = 4.4$ ($d = 500.0 \mu\text{m}$); dash-double dotted, $Db = 8.9$ ($d = 353.6 \mu\text{m}$); long dashed, $Db = 17.8$ ($d = 250.0 \mu\text{m}$); dash-dotted, $Db = 35.6$ ($d = 176.8 \mu\text{m}$); short dashed, $Db = 71.1$ ($d = 125.0 \mu\text{m}$); and solid line, $Db = 142.2$ ($d = 88.4 \mu\text{m}$).

$\bar{C}(x, y, z) > 10^{-4} \text{ kg/m}^3$. Note that the truncation of calculation at $\bar{C}(x, y, z) = 10^{-4} \text{ kg/m}^3$ for $\widehat{C}_{\text{RMS}}^l(x, y, z)$ is necessary in order to prevent division by zero and confine the statistical calculation within the mean surface oil plume. The threshold 10^{-4} kg/m^3 is found to be sufficiently small to not affect the statistics. Calculations using $5 \times 10^{-5} \text{ kg/m}^3$ and $2 \times 10^{-4} \text{ kg/m}^3$ as the threshold show negligible difference compared with the reported calculation.

As shown in Figure 1d, σ_c has insignificant dependence on La_t but varies monotonically as a function of Db : σ_c increases when Db decreases. To help categorize the parameter space, we also calculate the probability density function (PDF) of \tilde{C}/\bar{C} at $z = 0$ m and -6 m, where \bar{C} is the time-averaged value of \tilde{C} . As an example, we plot the PDFs for $La_t = 0.36$ and various Db values in Figure 3. We also calculate the horizontal-averaged oil concentration $\langle \tilde{C} \rangle$ for half of the domain ($0 \leq y \leq 500$ m) where the rising plume part is excluded. The distributions of \tilde{C} and $\langle \tilde{C} \rangle$ for $La_t = 0.36$ are shown in Figure 4.

For small droplets ($Db \gtrsim 25$), the surface oil slicks have low fingering level $\sigma_c < 1.0$ and are well diluted to form a smooth pattern (Figures 1i and 1j). Consistently, the PDFs of \tilde{C}/\bar{C} for cases $Db = 35.6 \sim 142.2$ in Figure 3 have a single and dominant peak close to $\tilde{C}/\bar{C} = 1.0$; the oil droplets are also well diluted vertically, presenting a fairly uniform distribution within the OML (Figures 4b and 4c). Conversely, oil plumes with

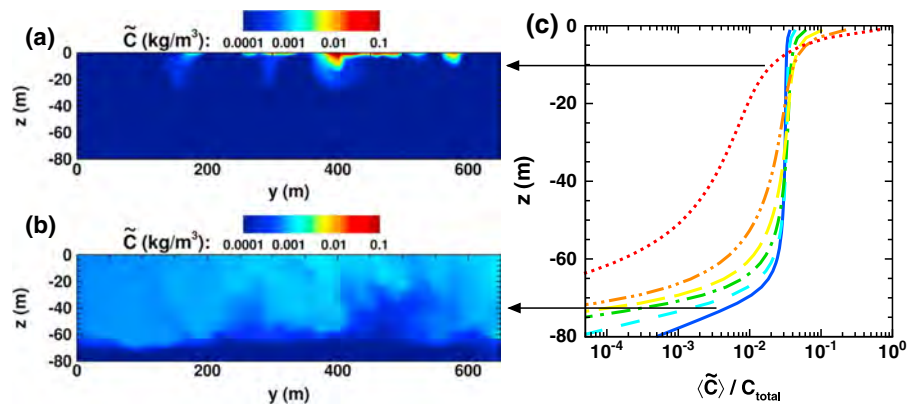


Figure 4. Vertical distribution of oil concentration in ocean mixed layer. (a) Contours of \tilde{C} at $x = 500$ m for case $(La_t, Db) = (0.36, 4.4)$ shown in Figure 1f. (b) Contours of \tilde{C} at $x = 700$ m for case $(La_t, Db) = (0.36, 142.2)$ shown in Figure 1j. (c) Vertical profiles of $\langle \tilde{C} \rangle$ normalized by its depth-averaged value over OML (calculation is done in $0 \leq y \leq 500$ m to exclude the rising oil plume part). The cases with $La_t = 0.36$ and various droplet diameters are plotted (see Figure 3 for caption).

$Db \lesssim 10$ have high fingering level $\sigma_c > 1.5$, indicating a temporal fluctuation of surface oil concentration that is apparently larger than its mean as a consequence of the strong downwind fingered pattern being transported crosswind over the surface (Figures 1e and 1f). The PDFs peak near $\tilde{C}/\bar{C} = 0$ corresponding to the gaps between the fingered oil slicks and display heavy tails corresponding to the high concentrations in the fingers (cases $Db = 4.4$ and 8.9 in Figure 3). Due to the strong buoyancy force when $Db \lesssim 10$, the vertical dilution of oil is inhibited, resulting in high concentrations near the surface that decays quickly with increasing depth (Figures 4a and 4c). For $10 \lesssim Db \lesssim 25$, the value of σ_c is moderate (between 1.0 and 1.5), corresponding to the blurred patterns shown in Figures 1g and 1h. Compared with other cases, the PDF for the case $Db = 17.8$ in Figure 3 is much flatter with a weak maximum near $\tilde{C}/\bar{C} = 0.5$ and a second peak near $\tilde{C}/\bar{C} = 0$. The vertical dilution of oil is also moderate as shown in Figure 4c.

The fingering level of the oil slicks in Figures 1a–1c can also be estimated based on image analysis, which gives $\sigma_c = 1.69$, 1.15 , and 0.46 , respectively (see section 4 in supporting information for details). Despite the lack of information on droplet size and flow conditions, the fingering levels in Figures 1a–1c are consistent with the fingered, blurred, and diluted categories evaluated based on the LES results (Figure 1d).

4. Conclusions

The combination of σ_c and PDFs of \tilde{C}/\bar{C} provides a quantitative approach to categorize the surface oil slick patterns into the three characteristic regimes (Figure 1d). The dominant dependence of σ_c on Db in our LES results suggests that it is the competition between buoyancy (rise velocity) and Langmuir circulation (downwelling velocity, characterized by U_s) that determines the surface oil slick characteristics. Therefore, Db essentially determines (i) the surface pattern of the slick (fingered, blurred, or diluted) and therefore the ratios between peak and average concentrations at the surface, (ii) the vertical depth of the plume, and (iii) the main direction of transport due to the combination of vertical mass distribution and the Ekman spiral.

LES results may suggest that the application of dispersants to surface oil slicks (which can significantly reduce the oil droplet size [National Research Council, 2005], increasing Db) may not only enhance the dilution of oil but also increase the crosswind transport of the plume. Moreover, the efficacy of dispersants applied at the surface is affected by how well they are mixed with the oil. If the dispersant and oil droplets are diluted at different levels and migrate along different paths (see e.g., Figure 1f versus Figure 1j and Figure 4a versus Figure 4b), dispersant efficiency can be reduced and its effects become more difficult to predict.

References

- Camilli, R., et al. (2010), Tracking hydrocarbon plume transport and biodegradation at Deepwater Horizon, *Science*, 330(6001), 201–204.
- Chamecki, M., and C. Meneveau (2011), Particle boundary layer above and downstream of an area source: Scaling, simulations, and pollen transport, *J. Fluid Mech.*, 683, 1–26.
- Chamecki, M., C. Meneveau, and M. B. Parlange (2008), A hybrid spectral/finite-volume algorithm for large-eddy simulation of scalars in the atmospheric boundary layer, *Boundary Layer Meteorol.*, 128(3), 473–484.
- Chamecki, M., C. Meneveau, and M. B. Parlange (2009), Large eddy simulation of pollen transport in the atmospheric boundary layer, *Boundary Layer Meteorol.*, 40(3), 241–255.
- Craik, A. D. D. (1985), *Wave Interactions and Fluid Flows*, Cambridge Univ. Press, Cambridge, U.K.
- Craik, A. D. D., and S. Leibovich (1976), A rational model for Langmuir circulations, *J. Fluid Mech.*, 73, 401–426.
- Edson, J., et al. (2007), The coupled boundary layers and air–sea transfer experiment in low winds, *Boundary Layer Meteorol.*, 88, 341–356.
- Ekman, V. W. (1905), On the influence of the Earth's rotation on ocean currents, *Ark. Mat. Astron. Fys.*, 2(11), 1–52.
- Garcia-Pineda, O., et al. (2013), Detection of floating oil anomalies from the Deepwater Horizon oil spill with synthetic aperture radar, *Oceanography*, 26(2), 124–137.
- Harcourt, R. R., and E. A. D'Asaro (2008), Large-eddy simulation of Langmuir turbulence in pure wind seas, *J. Phys. Oceanogr.*, 38(7), 1542–1562.
- Hasselmann, K., et al. (1973), Measurements of wind-wave growth and swell decay during the Joint North Sea Wave Project (JONSWAP), *Dtsch. Hydrogr. Z. Suppl.*, 8(12), 1–95.
- Hazen, T. C., et al. (2010), Deep-sea oil plume enriches indigenous oil-degrading bacteria, *Science*, 330(6001), 204–208.
- Kukulka, T., A. J. Plueddemann, J. H. Trowbridge, and P. P. Sullivan (2009), Significance of Langmuir circulation in upper ocean mixing: Comparison of observations and simulations, *Geophys. Res. Lett.*, 36(10), L10603, doi:10.1029/2009GL037620.
- Langmuir, I. (1938), Surface motion of water induced by wind, *Science*, 87(2250), 119–123.
- Leibovich, S. (1980), On wave–current interaction theories of Langmuir circulations, *J. Fluid Mech.*, 99, 715–724.
- Leibovich, S. (1983), The form and dynamics of Langmuir circulation, *Annu. Rev. Fluid Mech.*, 15, 391–427.
- Leifer, I., et al. (2012), State of the art satellite and airborne marine oil spill remote sensing: Application to the BP Deepwater Horizon oil spill, *Remote Sens. Environ.*, 124, 185–209.
- Lenn, Y.-D., and T. K. Chereskin (2009), Observations of Ekman currents in the Southern Ocean, *J. Phys. Oceanogr.*, 39(3), 768–779.
- Li, M. (2000), Estimating horizontal dispersion of floating particles in wind-driven upper ocean, *Spill Sci. Technol. Bull.*, 6(3–4), 255–261.
- Li, M., C. Garrett, and E. Skillingstad (2005), A regime diagram for classifying turbulent large eddies in the upper ocean, *Deep Sea Res. Part I*, 52(2), 259–278.

Acknowledgments

This research was supported by the Gulf of Mexico Research Initiative RFP-II.

The Editor thanks two anonymous reviewers for their assistance in evaluating this paper.

- McWilliams, J. C., and P. P. Sullivan (2000), Vertical mixing by Langmuir circulation, *Spill Sci. Technol. Bull.*, 6(3–4), 225–237.
- McWilliams, J. C., P. P. Sullivan, and C.-H. Moeng (1997), Langmuir turbulence in the ocean, *J. Fluid Mech.*, 334, 1–30.
- Moum, J. N., and W. D. Smyth (2001), Upper ocean mixing processes, encyclopedia of ocean sciences, vol. 6, 3093–3100, Academic Press, Waltham, Mass.
- Committee on Understanding Oil Spill Dispersants: Efficacy and Effects, and National Research Council (2005), *Oil Spill Dispersants: Efficacy and Effects*, The National Academies Press, Washington, D. C.
- Noh, Y., I. S. Kang, M. Herold, and S. Raasch (2006), Large eddy simulation of particle settling in the ocean mixed layer, *Phys. Fluids*, 18(8), 085109.
- Okubo, A. (1970), Horizontal dispersion of floatable particles in the vicinity of velocity singularity such as convergences, *Deep Sea Res.*, 17(3), 445–454.
- Pan, Y., M. Chamecki, and S. A. Isard (2013), Dispersion of heavy particles emitted from area sources in the unstable atmospheric boundary layer, *Boundary Layer Meteorol.*, 146(2), 235–256.
- Rye, H. (2000), Probable effects of Langmuir circulation observed on oil slicks in the field, *Spill Sci. Technol. Bull.*, 6(3–4), 263–271.
- Simecek-Beatty, D., and W. J. Lehr (2000), Langmuir circulation and oil spill trajectory models workshop - Comments and recommendations, *Spill Sci. Technol. Bull.*, 6(3–4), 273–274.
- Skyllingstad, E. D., and D. W. Denbo (1995), An ocean large-eddy simulation of Langmuir circulations and convection in the surface mixed layer, *J. Geophys. Res.*, 100(C5), 8501–8522.
- Stokes, G. G. (1847), On the theory of oscillatory waves, *Trans. Camb. Phil. Soc.*, 8, 441–455.
- Sullivan, P. P., and J. C. McWilliams (2010), Dynamics of winds and currents coupled to surface waves, *Annu. Rev. Fluid Mech.*, 42, 19–42.
- Teixeira, M. A. C., and S. E. Belcher (2010), On the structure of Langmuir turbulence, *Ocean Model.*, 31(3–4), 105–119.
- Thorpe, S. A. (2004), Langmuir circulation, *Annu. Rev. Fluid Mech.*, 36, 55–79.

Erratum

In the originally published version of this article, several instances of the supporting information text were incorrectly presented. The following have since been corrected and this version may be considered the authoritative version of record.

In equations 2 and 6 in the supporting information, ρ has been changed to θ .

Supporting Information to “Inhibition of oil plume dilution in Langmuir ocean circulation (DOI: 10.1002/2014GL059284)”

Di Yang¹, Marcelo Chamecki², and Charles Meneveau^{*1}

¹Center for Environmental and Applied Fluid Mechanics, Johns Hopkins University, Baltimore, Maryland 21218, USA

²Department of Meteorology, The Pennsylvania State University, University Park, Pennsylvania 16802, USA

This document contains a throughout introduction to our large eddy simulation model, as well as additional results as validations of our simulation and analysis approach.

1 Full Methods for Large Eddy Simulation

In recent years, large eddy simulation (LES) based on the Craik–Leibovich (CL) equations has become a promising numerical tool for the simulation of Langmuir turbulence in the ocean mixed layer (*Thorpe, 2004; Sullivan and McWilliams, 2010*). The LES model we use is based on the filtered CL equations (*Leibovich, 1980, 1983; Craik, 1985*). It accounts for the phase-averaged effects of surface gravity waves on the mean flow and turbulence by including a (uniform and constant) Stokes drift term. This approach has been used successfully in LES studies of Langmuir turbulence before (e.g. *Skyllingstad and Denbo, 1995; McWilliams et al., 1997; McWilliams and Sullivan, 2000; Li et al., 2005; Polton et al., 2005; Noh et al., 2006; Harcourt and D’Asaro, 2008; Noh et al., 2009; Grant and Belcher, 2009; Kukulka et al., 2009, 2013*). The buoyancy effects due to fluctuations in density (represented by potential temperature) and oil droplet concentrations are included in the momentum equation based on the Boussinesq approximation. In our LES model, the equations describing the resolved velocity field are

$$\nabla \cdot \tilde{\mathbf{u}} = 0, \quad (1)$$

$$\begin{aligned} \frac{\partial \tilde{\mathbf{u}}}{\partial t} + (\tilde{\mathbf{u}} \cdot \nabla) \tilde{\mathbf{u}} = & -\frac{1}{\rho_0} \nabla \tilde{p} - f \mathbf{e}_3 \times \tilde{\mathbf{u}} + \mathbf{u}_s \times (f \mathbf{e}_3 + \nabla \times \tilde{\mathbf{u}}) - \nabla \cdot \boldsymbol{\tau} \\ & - \left(1 - \frac{\tilde{\theta}}{\langle \theta \rangle}\right) g \mathbf{e}_3 + \left(1 - \frac{\rho_d}{\rho_0}\right) \frac{\tilde{C}}{\rho_d} g \mathbf{e}_3. \end{aligned} \quad (2)$$

Here, tilde denotes a resolved variable, $\langle \cdot \rangle$ denotes horizontal averaging, \mathbf{u} is the fluid velocity, ρ_d is the density of oil, ρ_0 is the reference sea water density, θ is the temperature, p is the modified pressure, \tilde{C} is the resolved mass concentration of oil, g is the acceleration of gravity, f is the Coriolis frequency, \mathbf{e}_3 is the unit vector in the vertical direction, \mathbf{u}_s is the Stokes drift velocity, and $\boldsymbol{\tau} = (\tilde{\mathbf{u}}\tilde{\mathbf{u}} - \tilde{\mathbf{u}}\tilde{\mathbf{u}})$ is the subgrid-scale (SGS) stress tensor. The first four terms on the right-hand side of equation (2) are pressure gradient force, Coriolis force, the vortex force due to Stokes drift representing the phase-averaged effects of surface gravity waves on the mean flow and turbulence, and the SGS term representing the effect of fluid motions at small, unresolved scales. The last two terms in equation (2) are the buoyancy force due to temperature fluctuations and due to oil concentration, respectively.

*Email: meneveau@jhu.edu

For a sinusoidal wave that propagates in the x -direction, i.e.

$$\eta(x, t) = a \cos[kx - \omega t], \quad (3)$$

$$u_w(x, t) = a\omega e^{kz} \cos[kx - \omega t], \quad (4)$$

where η is the wave elevation and u_w is the wave orbital velocity, the corresponding Stokes drift velocity is given by (Stokes, 1847)

$$\mathbf{u}_s(z) = \mathbf{e}_1 U_s e^{2kz}. \quad (5)$$

Here, $U_s = \omega ka^2$ is the magnitude of the wave-induced Stokes-drift, k is the wavenumber, ω is the angular frequency ($\omega = \sqrt{gk}$ for deep-water wave), a is the wave amplitude, and \mathbf{e}_1 is the unit vector in the streamwise (wave propagation) direction.

The water temperature field is governed by a filtered convection–diffusion equation,

$$\frac{\partial \tilde{\theta}}{\partial t} + (\tilde{\mathbf{u}} + \mathbf{u}_s) \cdot \nabla \tilde{\theta} = -\nabla \cdot \boldsymbol{\pi}_\theta, \quad (6)$$

where $\boldsymbol{\pi}_\theta = (\tilde{\mathbf{u}}\tilde{\theta} - \tilde{\mathbf{u}}\tilde{\theta})$ is the SGS temperature flux. The concentration field of oil droplets of dimension d is described by a continuous Eulerian function $C(\mathbf{x}, t; d)$. The conservation of oil mass yields an evolution equation for C . Its filtered version is given by

$$\frac{\partial \tilde{C}}{\partial t} + (\tilde{\mathbf{v}} + \mathbf{u}_s) \cdot \nabla \tilde{C} = -\nabla \cdot \boldsymbol{\pi}_c + Q_s, \quad (7)$$

where \mathbf{v} is the velocity of the oil droplet phase, Q_s is a source term representing the oil plume e.g. being released from an underwater blowout (see § 3 in this file), and $\boldsymbol{\pi}_c = (\tilde{\mathbf{u}}\tilde{C} - \tilde{\mathbf{u}}\tilde{C})$ is the SGS oil concentration flux. The resolved oil droplet velocity is given by (Ferry and Balachandar, 2001)

$$\tilde{\mathbf{v}} = \tilde{\mathbf{u}} - w_r \mathbf{e}_3 + (R - 1) \tau_d \left(\frac{D\tilde{\mathbf{u}}}{Dt} + \nabla \cdot \boldsymbol{\tau} \right), \quad (8)$$

where $w_r = (\rho_d - \rho_0)gd^2/(18\mu_f)$ is the droplet rising velocity with μ_f being the viscosity of water, \mathbf{e}_3 is the unit vector in the vertical direction, $R = 3\rho_0/(2\rho_d + \rho_0)$ is the acceleration parameter, and $\tau_d = (\rho_d + \rho_0/2)d^2/(18\mu_f)$ is the droplet time scale.

The set of equations is closed by adopting subgrid-scale models for the SGS terms $\boldsymbol{\tau}$, $\boldsymbol{\pi}_\theta$ and $\boldsymbol{\pi}_c$. The SGS stress tensor $\boldsymbol{\tau}$ is parameterized using the Lilly–Smagorinsky model (Smagorinsky, 1963; Lilly, 1967). It uses viscous analogy and the mixing length approach and expresses the SGS stress tensor as $\tau_{ij}^{smag} = -2\nu_T \tilde{S}_{ij} = -2(c_s \Delta)^2 |\tilde{S}| \tilde{S}_{ij}$, where $\tilde{S}_{ij} = (\partial \tilde{u}_i / \partial x_j + \partial \tilde{u}_j / \partial x_i) / 2$ is the resolved strain rate tensor, ν_T is the SGS eddy viscosity, and Δ is the grid (filter) scale. The only unknown, the Smagorinsky coefficient c_s , is flow and situation dependent. A widely used approach to evaluate c_s in LES is the dynamic SGS model (Germano et al., 1991), which uses the resolved scales (at scale 2Δ) to “measure” the model coefficient c_s during the simulation. This model uses the assumption of scale-invariance by applying c_s measured from the resolved scales to the subgrid-scale range. However, the scale-invariance does not hold when the grid-filter scale Δ tends to the integral scale, as occurs in the first few simulation grid-points near the surface of the ocean mixed layer. Porté-Agel et al. (2000) included the scale-dependence of c_s into the dynamic SGS model by considering an additional filtering operation at a scale 4Δ , and dynamically measure the scale-dependence of c_s at 2Δ and 4Δ .

When evaluating c_s using the dynamic model, spatial averaging operation is required to reduce numerical oscillations in the model coefficient. However, the spatial averaging is not proper for the current problem because of the strong spatial non-uniformity of the ocean mixed layer induced by the Langmuir circulations and the buoyancy of the oil plume. For such complex flows, Meneveau et al. (1996) introduced the Lagrangian approach in which time-averaging following fluid trajectories replaces spatial averaging. Both the scale-dependence and Lagrangian averaging approaches have been combined to yield the Lagrangian scale-dependent dynamic SGS model (Bou-Zeid et al., 2005), which is used to determine c_s in the current LES framework. This model has been validated in detail with data (Bou-Zeid et al., 2005; Kumar et al., 2010). In the present work, the advection

velocity in the Lagrangian averaging includes the Stokes drift velocity. The SGS fluxes π_θ and π_c are modeled using flux-gradient model, i.e. $\pi_\theta = (\nu_T/\text{Pr}_T)\nabla\tilde{\theta}$ and $\pi_c = (\nu_T/\text{Sc}_T)\nabla\tilde{C}$ with constant turbulent Prandtl number $\text{Pr}_T = 0.4$ and Schmidt number $\text{Sc}_T = 0.8$.

By adopting the aforementioned subgrid-scale models for τ , π_θ and π_c and specifying the Stokes drift velocity, the set of equations (1), (2), (6) and (7) are closed. They are then discretized on a Cartesian grid and solved by computer simulation. In particular, equations (1), (2) and (6) are discretized by a hybrid method, with Fourier-series based pseudo-spectral method on a collocated grid in the horizontal (homogeneous) directions and a second order centred finite difference method on a staggered grid in the vertical (inhomogeneous) direction. The second-order Adams–Bashforth scheme is used for the time integration. A projection method is used to enforce the incompressibility constraint. This is done by solving the Poisson’s equation for pressure and then projecting the calculated velocity field to a divergence-free velocity field using the pressure correction. Because the oil plume distribution is highly inhomogeneous, a pseudo-spectral method for spatial discretization is avoided since it often causes unphysical solutions such as localized regions of negative (unphysical) oil concentrations. To avoid these problems, *Chamecki et al.* (2008) developed a hybrid pseudo-spectral and finite-volume algorithm for the LES of particle dispersion in geophysical flows. In this method, a specially designed interpolation scheme is used to interpolate the velocity field from the pseudo-spectral and finite-difference grid to the finite-volume grid for oil. The oil concentration is then simulated using a finite-volume method with the advection term being calculated using the bounded third-order upwind interpolation scheme SMART (*Gaskell and Lau*, 1988). This hybrid scheme has been used in a number of prior LES studies of particle and scalar dispersion in geophysical flows (*Chamecki et al.*, 2008, 2009; *Chamecki and Meneveau*, 2011; *Pan et al.*, 2013).

In the simulation, we use a constant Coriolis frequency $f = 7 \times 10^{-5} \text{s}^{-1}$ (corresponding to a latitude of 28.7°N), and a potential temperature field to represent density stratification (*McWilliams et al.*, 1997). The initial potential temperature profile is well-mixed in the OML ($0 \geq z > -100 \text{m}$), and it is stably stratified below with a temperature gradient $d\theta/dz = 0.01 \text{K m}^{-1}$. A heat flux of $Q = -15 \text{W m}^{-2}$ is imposed at the surface. We perform LES in a domain 1000 m long and wide and 300 m deep. The domain is discretized using $100 \times 100 \times 145 = 1.45 \times 10^6$ points and a timestep of 0.1 s.

2 Effect of turbulent Langmuir number on the Langmuir turbulence and comparison with prior LES

In the simulation, we consider four wave conditions with wavelengths $\lambda = 15, 30, 60$ and 120m . With a fixed wave steepness $2\pi a/\lambda = 0.084$, these four conditions have wave amplitudes $a = 0.2, 0.4, 0.8$ and 1.6m , corresponding to World Meteorological Organization sea state classifications 2, 3, 4 and 5, respectively. For fixed wave steepness, the Stokes drift velocity $U_s = \sqrt{g\lambda/2\pi}(2\pi a/\lambda)^2$ (where $g = 9.81 \text{m/s}^2$ is the acceleration of gravity) increases as the wavelength increases. The corresponding turbulent Langmuir numbers for these four wave cases are $La_t = 0.61, 0.51, 0.43$ and 0.36 .

Figure 1 illustrates the effect of Stokes drift on the Langmuir turbulence. For a fixed wind condition, stronger Stokes drift (corresponding to smaller La_t) results in stronger Langmuir circulations, indicated by the larger vertical velocity in Figure 1a–1c. Figure 1d shows the depth-averaged vertical velocity variance σ_w^2 as a function of La_t . The value of σ_w^2/u_*^2 decreases rapidly as La_t increases for Langmuir turbulence ($La_t < 0.7$), but remains nearly constant for shear turbulence ($La_t > 0.7$). Despite small differences likely caused by differences in flow configuration (such as magnitude of surface heat fluxes), our LES result shows good agreement with the LES results presented by *Li et al.* (2005).

3 The choice of oil mass flow rate and droplet diameter

We study a canonical problem to address the fundamental question of how oil droplets are diluted within the ocean mixed layer. We release the oil from a localized source (with a $10 \times 10 \text{m}^2$ effective cross-section area as determined by the grid resolution) at 150 m depth. This value falls in the range of the predicted value by the Double-Plume Integral Model (*Socolofsky et al.*, 2008, 2011), which shows that the radius of the width of an oil plume from a deep-water blowout varies within the range of $1 \sim 25 \text{m}$. This configuration mimics a rising oil

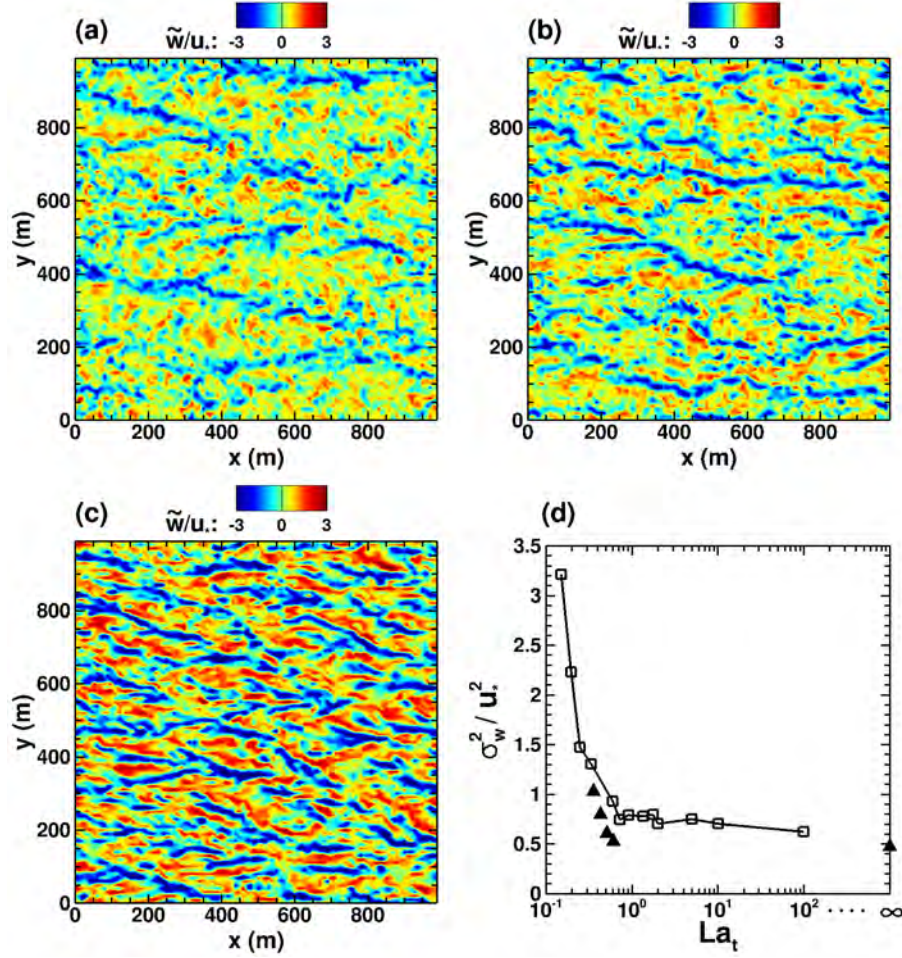


Figure 1: Effect of La_t on the Langmuir turbulence. Contours of instantaneous vertical velocity on the horizontal plane at $z = -10$ m are plotted for various cases: (a), $La_t = 0.61$; (b) $La_t = 0.51$; and (c) $La_t = 0.36$. (d) Depth-averaged (from the surface to the thermocline) vertical velocity variance is plotted as a function of La_t : \square , LES results from *Li et al.* (2005); and \blacktriangle , the current LES results. Note that in (d), the x -axis extends to infinity to include a pure shear turbulence case with $U_s = 0$ for the current LES.

plume that passes through the region of injection with a cross-section having a diameter of approximately 10 m. We use an oil mass flow rate of $Q_s = 1$ kg/s, corresponding to a volumetric flow rate of 0.0012 m³/s for oil with density 859.9 kg/m³.

We remark that the oil flow rate Q_s used in our LES is smaller than the total release rates found in many real oil spill situations. However, the oil release rate varies a lot for different events. For example, in the DeepSpill Plumes field experiment the oil was released from 844 m depth with a rate of 0.017 m³/s; in the Deepwater Horizon event, the oil was released from 1503 ~ 1514 m with a rate of $0.06 \sim 0.11$ m³/s. During a specific event, the oil release rate also varies significantly with time. When the plumes rise over various layers of sea water, phenomena such as intrusion formation and the cross-current induced plume separation can significantly reduce the remaining oil flow rate before the plumes reach the ocean mixed layer (*Socolofsky et al.*, 2011). Moreover, it is a challenging and open research topic to accurately determine the droplet size distribution in an oil plume. Therefore, an accurate estimation of oil release rates for each individual droplet size in the plume is not available. Therefore, the oil flow rate $Q_s = 1$ kg/s used in this study may be relatively small for some droplet sizes but large for others. We thus simply choose a single constant Q_s for all the different droplet sizes, so that the corresponding LES results can be compared directly, without being affected by additional parameters.

The distribution of oil droplet size in deep-water blowout plumes is difficult to measure or estimate (Chen and Yapa, 2007). The segregation of plumes with various droplet sizes (Socolofsky and Adams, 2002) as well as the breakup and coalescence of droplets (Davis, 1999) further complicate the situation. For the purposes of the present study, it is reasonable to consider each fixed and single droplet size separately, in order to develop understanding of the underlying most relevant mechanisms. For each Langmuir turbulence condition, we consider six ($n = 1 \sim 6$) oil droplet diameters $d(n) = 88.4 \times 2^{(n-1)/2} \mu\text{m}$. Based on Stokes' law, the rise velocity of a small oil droplet with effective diameter d is given by $w_r = (\rho_d - \rho)gd^2/(18\mu_f)$. This expression for w_r assumes small enough droplets for the Stokes flow drag formula to be valid (Clift et al., 1978; Elliot et al., 1986; Zhang and Yapa, 2000), typically for $d \lesssim 1$ mm for oil droplets. Therefore, the corresponding rise velocities for the six different diameters are $w_r(n) = 0.000675 \times 2^{n-1}$ m/s. Thus the 24 LES cases in this paper cover a wide range for the drift-to-buoyancy parameter Db , from 1.6 to 142.2.

4 Estimation of fingering level from field oil spill photos

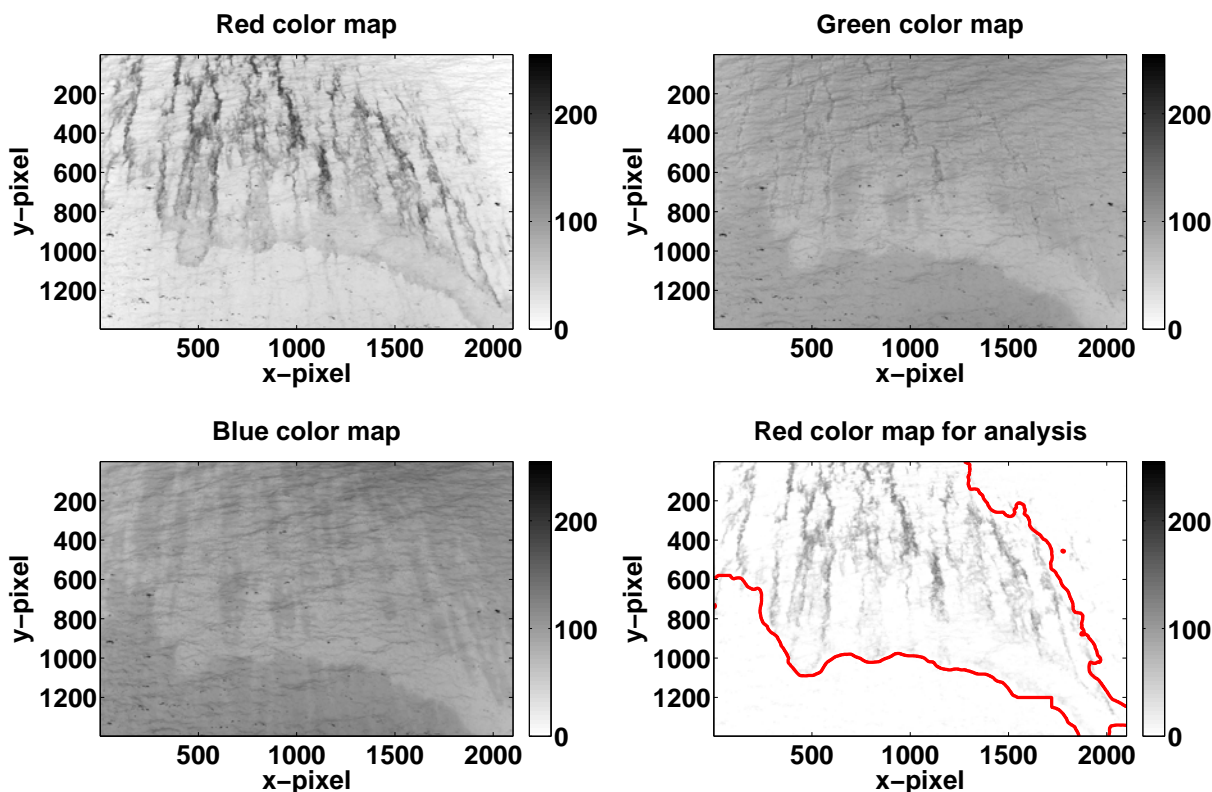


Figure 2: Digitized RGB color maps of Figure 1a: top-left panel, red color map; top-right panel, green color map; and bottom-left panel, blue color map. The bottom-right panel shows the refined red color map with the removal of the background red color (estimated based on the values in the no-oil regions). The sampling area for statistical analysis is indicated by the thick red line.

Field or laboratory studies of oil spill dispersion in Langmuir turbulence are very challenging. For laboratory studies, most of the efforts to date have been devoted to dye dispersion in finite-size wind-wave tanks (e.g. Faller and Caponi, 1978; Melville et al., 1998), as well as crude oil dispersion in simple stratified flow with/without a crossflow (e.g. Socolofsky and Adams, 2002, 2005). Field observations can produce valuable information in realistic ocean conditions based on satellite and aerial remote sensing of surface oil slicks (see reviews by Fingas

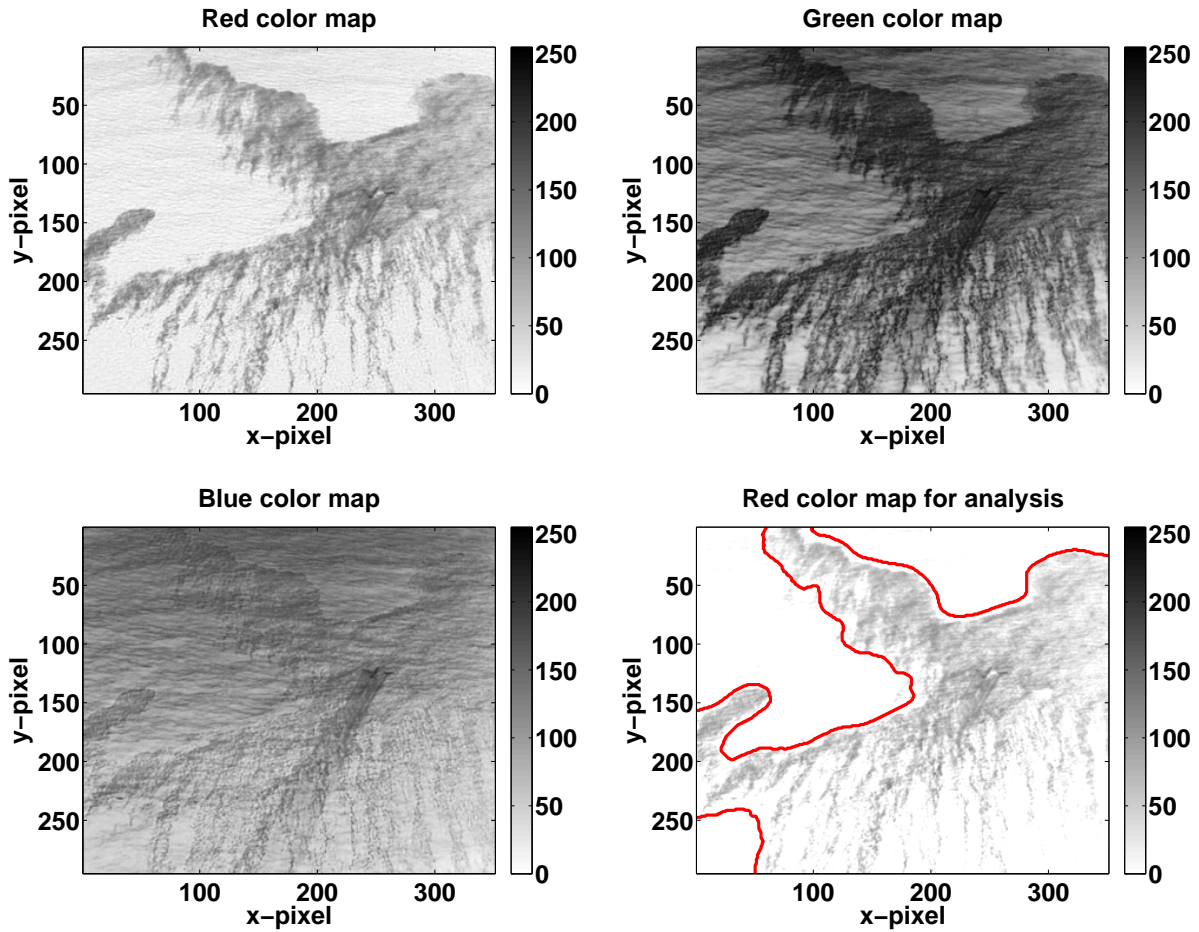


Figure 3: Digitized RGB color maps of Figure 1b. The details of the figure caption are the same as in Figure 2.

and Brown, 2011; Leifer et al., 2012), but details of the flow field information are usually lacking. We note that in a field experiment reported by Rye (2000), the observed surface oil slick pattern from an underwater spill (as indicated by the ultraviolet and infrared images in their Figures 4 and 5) showed consistent features as those obtained from our LES (see Figures 1 and 2 in the main paper), i.e. downwind fingers and crosswind mean transport.

Moreover, a comparison of the fingering level can be made between the LES results and the oil slicks recorded in the aerial images in Figure 1a–1c. To do so, the original images are digitized, with the color for each pixel being described by the RGB code (Hunt, 2004). Using the RGB code, the original image is decomposed into three basic colors, red (R), green (G) and blue (B), which are described by integer numbers ranging from 0 to 255. As shown in Figures 2–4, the maps of the red color code R provide the best representation of the observed oil slick patterns in Figures 1a–1c. Therefore, they are used for the statistical estimation of the fingering level.

First, a linear spatial filtering is performed for the red color code, i.e. the filtered value R_f for each pixel equals to the average of the unfiltered values R in a ($15 \text{ pixel} \times 15 \text{ pixel}$) area centered at the pixel. By choosing a proper threshold based on R_f , a sampling area for estimating σ_c is obtained (e.g. the thick red lines in the bottom-right panel of Figure 2). The red color map is further refined by removing the background value estimated based on the no-oil areas. This is particularly necessary for the analysis of Figure 1c, in which a significant background bias exists (see the top-left panel in Figure 4). With the refined red color maps shown in the bottom-right panel of Figures 2–4, the fingering levels σ_c of the photographed oil slicks are estimated following a similar process as

described in Section 3 of the main paper. Note that because only a single snapshot is available, here spatial instead of temporal averaging is used for the analysis of the LES results and definition of fluctuations. As a result, the estimated fingering levels are $\sigma_c = 1.69, 1.15, \text{ and } 0.46$ for Figures 1a–1c, respectively, which are consistent with the values obtained from our LES as shown in Figure 1d.

References

- Bou-Zeid, E., C. Meneveau, and M. B. Parlange (2005), A scale-dependent Lagrangian dynamic model for large eddy simulation of complex turbulent flows, *Phys. Fluids*, *17*(2), 025105.
- Chamecki, M., and C. Meneveau (2011), Particle boundary layer above and downstream of an area source: scaling, simulations, and pollen transport, *J. Fluid Mech.*, *683*, 1–26.
- Chamecki, M., C. Meneveau, and M. B. Parlange (2008), A hybrid spectral/finite-volume algorithm for large-eddy simulation of scalars in the atmospheric boundary layer, *Boundary-Layer Meteorol.*, *128*(3), 473–484.
- Chamecki, M., C. Meneveau, and M. B. Parlange (2009), Large eddy simulation of pollen transport in the atmospheric boundary layer, *Boundary-Layer Meteorol.*, *40*(3), 241–255.
- Chen, F., P. D. Yapa (2007), Estimating the oil droplet size distributions in deepwater oil spills, *J. Hydraul. Res.*, *133*(2), 197–207.
- Clift, R., J. R. Grace, and M. E. Weber (1978), *Bubbles, Drops, and Particles*, Academic, New York.
- Craik, A. D. D. (1985), *Wave Interactions and Fluid Flows*, Cambridge Univ. Press, Cambridge.
- Davis, R. H. (1999), Buoyancy-driven viscous interaction of a rising drop with a smaller trailing drop, *Phys Fluids*, *11*(5), 1016–1028.
- Elliot, A. J., N. Hurford, and C. J. Penn (1986), Shear diffusion and the spreading of oil slicks, *Mar. Pollut. Bull.*, *17*(7), 308–313.
- Faller, A. J., and E. A. Caponi (1978), Laboratory studies of wind-driven Langmuir circulations, *J. Geophys. Res.*, *83*(C7), 3617–3633.
- Ferry, J., and S. Balachandar (2001), A fast Eulerian method for disperse two-phase flow, *Int. J. Multiphase Flow*, *27*(7), 1199–1226.
- Fingas, M., and C. E. Brown, (2011), Oil spill remote sensing: A review, in *Oil spill science and technology*, Gulf Professional Publishing, Boston, 111–169.
- Gaskell, P. H., and A. K. C. Lau (1988), Curvature-compensated convective transport: SMART, a new boundedness-preserving transport algorithm, *Int. J. Numer. Methods Fluids*, *8*(6), 617–641.
- Germano, M., U. Piomelli, P. Moin, and W. H. Cabot (1991), A dynamic subgrid-scale eddy viscosity model, *Phys. Fluids A* *3*(7), 1760–1785.
- Grant, A. L. M., and S. E. Belcher (2009), Characteristics of Langmuir turbulence in the ocean mixed layer, *J. Phys. Oceanogr.*, *39*(8), 1871–1887.
- Harcourt, R. R., and E. A. D’Asaro (2008), Large-eddy simulation of Langmuir turbulence in pure wind seas, *J. Phys. Oceanogr.*, *38*(7), 1542–1562.
- Hunt, R. W. G. (2004), *The Reproduction of Colour*, 6th Edition, in *Wiley-IS&T Series in Imaging Science and Technology*, Wiley, Chichester.
- Kukulka, T., A. J. Plueddemann, and P. P. Sullivan (2013), Inhibited upper ocean restratification in nonequilibrium swell conditions, *Geophys. Res. Lett.*, *40*(14), 3672–3676.

- Kukulka, T., A. J. Plueddemann, J. H. Trowbridge, and P. P. Sullivan (2009), Significance of Langmuir circulation in upper ocean mixing: Comparison of observations and simulations, *Geophys. Res. Lett.*, *36*(10), L10603.
- Kumar, V., G. Svensson, A. A. Holtslag, C. Meneveau, and M. B. Parlange (2010), Impact of surface flux formulations and geostrophic forcing on large-eddy simulations of diurnal atmospheric boundary layer flow, *J. Appl. Meteor. Climatol.* *49*(7), 1496–1516.
- Leibovich, S. (1980), On wave–current interaction theories of Langmuir circulations, *J. Fluid Mech.*, *99*, 715–724.
- Leibovich, S. (1983), The form and dynamics of Langmuir circulation, *Annu. Rev. Fluid Mech.*, *15*, 391–427.
- Leifer, I., W. J. Lehr, D. Simecek-Beatty, E. Bradley, R. Clark, P. Dennison, Y. Hu, S. Matheson, C. E. Jones, B. Holt, M. Reif, D. A. Roberts, J. Svejksky, G. Swayze, and J. Wozencraft (2012), State of the art satellite and airborne marine oil spill remote sensing: Application to the BP *Deepwater Horizon* oil spill, *Remote Sens. Environ.*, *124*, 185–209.
- Li, M., C. Garrett, and E. Skillingstad (2005), A regime diagram for classifying turbulent large eddies in the upper ocean, *Deep-Sea Res. I*, *52*(2), 259–278.
- Lilly, D. K. (1967), The representation of small-scale turbulence in numerical simulation experiments, In *Proc IBM Scientific Computing Symposium on Environmental Science*, 195–210.
- McWilliams, J. C., and P. P. Sullivan (2000), Vertical mixing by Langmuir circulation, *Spill Sci. Technol. B.*, *6*(3–4), 225–237.
- McWilliams, J. C., P. P. Sullivan, and C.-H. Moeng (1997), Langmuir turbulence in the ocean, *J. Fluid Mech.*, *334*, 1–30.
- Melville, W. K., R. Shear, and F. Veron (1998), Laboratory measurements of the generation and evolution of Langmuir circulations, *J. Fluid Mech.*, *364*, 31–58.
- Meneveau, C., T. Lund, and W. Cabot (1996), A Lagrangian dynamic subgrid-scale model of turbulence, *J. Fluid Mech.*, *319*, 353–385.
- Noh, Y., G. Goh, S. Raasch, and M. Gryscha (2009), Formation of a diurnal thermocline in the ocean mixed layer simulated by LES, *J. Phys. Oceanogr.*, *39*(5), 1244–1257.
- Noh, Y., I. S. Kang, M. Herold, and S. Raasch (2006), Large eddy simulation of particle settling in the ocean mixed layer, *Phys. Fluids*, *18*(8), 085109.
- Pan, Y., M. Chamecki, and S. A. Isard (2013), Dispersion of heavy particles emitted from area sources in the unstable atmospheric boundary layer, *Boundary-Layer Meteorol.*, *146*(2), 235–256.
- Polton, J. A., D. M. Lewis, and S. E. Belcher (2005), The role of wave-induced Coriolis–Stokes forcing on the wind-driven mixed layer, *J. Phys. Oceanogr.*, *35*(4), 444–457.
- Porté-Agel, F., C. Meneveau, and M. B. Parlange (2000), A dynamic scale dependent model for large eddy simulation: Application to the atmospheric boundary layer, *J. Fluid Mech.*, *415*, 261–284.
- Rye, H. (2000), Probable effects of Langmuir Circulation observed on oil slicks in the field, *Spill Sci. Technol. B.*, *6*(3–4), 263–271.
- Skyllingstad, E. D., and D. W. Denbo (1995), An ocean large-eddy simulation of Langmuir circulations and convection in the surface mixed layer, *J. Geophys. Res.*, *100*(C5), 8501–8522.
- Socolofsky, S. A., and E. E. Adams (2002), Multi-phase plumes in uniform and stratified crossflow, *J. Hydraul. Res.* *40*(6), 661–672.
- Socolofsky, S. A., and E. E. Adams (2005), Role of slip velocity in the behavior of stratified multiphase plumes, *J. Hydraul. Eng.* *131*(4), 273–282.

- Socolofsky, S. A., E. E. Adams, and C. R. Sherwood (2011), Formation dynamics of subsurface hydrocarbon intrusions following the Deepwater Horizon blowout. *Geophys. Res. Lett.*, 38(9), L09602.
- Socolofsky, S. A., T. Bhaumik, and D.-G. Seol (2008), Double-plume integral models for near-field mixing in multiphase plumes, *J. Hydraul. Eng.*, 134(6), 772–783.
- Smagorinsky, J. (1963), General circulation experiments with the primitive equations. I. the basic experiment, *Mon. Weather Rev.*, 91(3), 99–164.
- Stokes, G. G. (1847), On the theory of oscillatory waves, *Trans. Camb. Philos. Soc.*, 8, 441–455.
- Sullivan, P. P., and J. C. McWilliams (2010), Dynamics of winds and currents coupled to surface waves, *Annu. Rev. Fluid Mech.*, 42, 19–42.
- Thorpe, S. A. (2004), Langmuir circulation, *Annu. Rev. Fluid Mech.*, 36, 55–79.
- Zhang, L., and P. D. Yapa (2000), Buoyant velocity of spherical and nonspherical bubbles/droplets, *J. Hydraul. Eng.*, 126(11), 852–854.

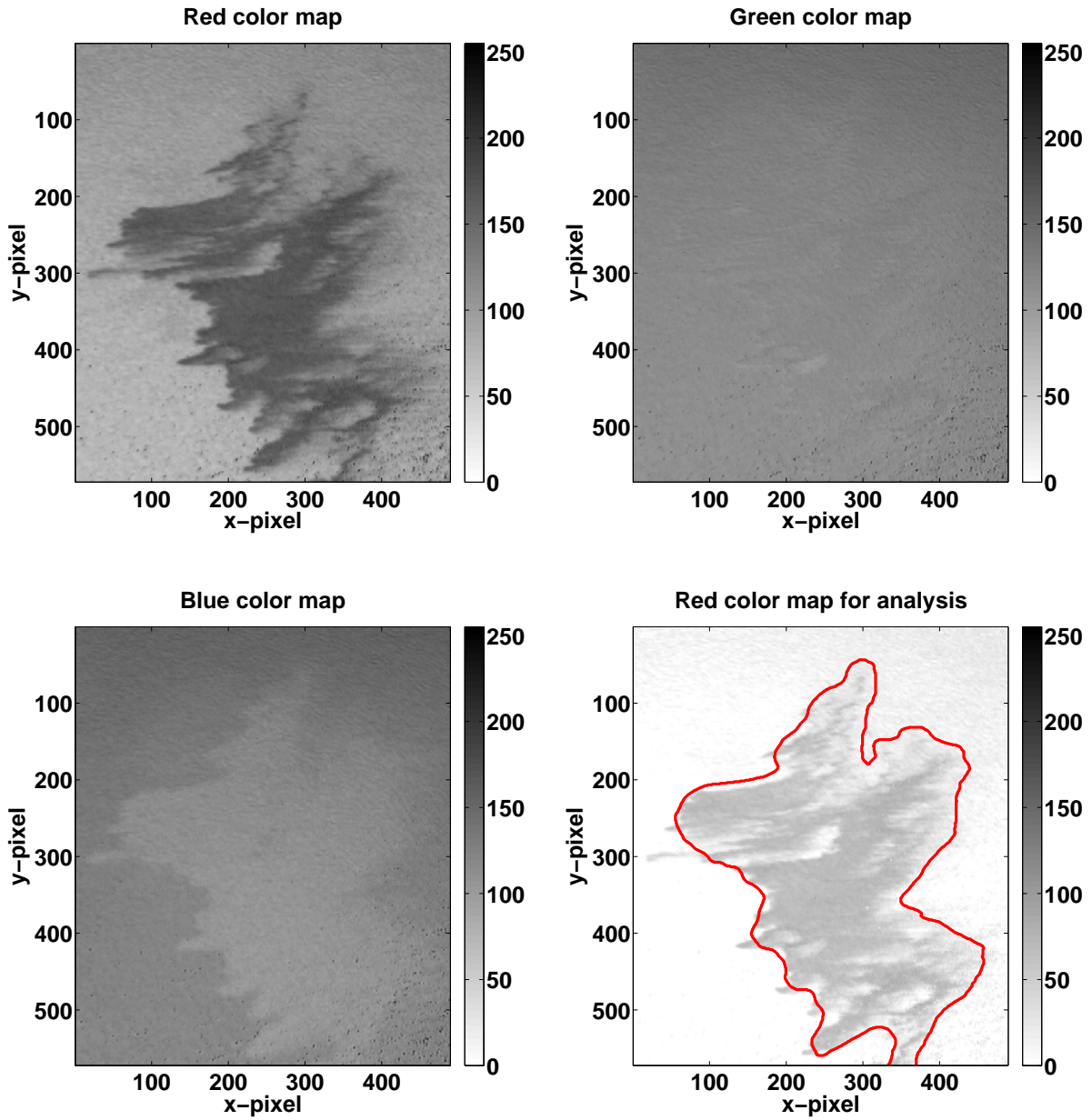


Figure 4: Digitized RGB color maps of Figure 1c. The details of the figure caption are the same as in Figure 2.